# Climate Impacts of Parameterizing Subgrid Variation and Partitioning of Land Surface Heat Fluxes to the Atmosphere with the NCAR CESM1.2

Ming Yin[1], Yong Wang[1], Wenqi Sun[1], Jianbo Deng[1,2], Daoming Wei[1], Ying Kong[3], Bin Wang[1,4,5]

5  [1]Department of Earth System Science, Ministry of Education Key Laboratory for Earth System Modeling, Institute for Global Change Studies, Tsinghua University, Beijing, 100084 China
[2]Hunan Institute of Meteorological Sciences, Changsha, 410118 China
[3]College of Atmospheric Sciences, Lanzhou University, Lanzhou, 730000 China
[4]State Key Laboratory of Numerical Modeling for Atmospheric Sciences and Geophysical Fluid Dynamics, Institute of
10  Atmospheric Physics, Chinese Academy of Sciences, Beijing, 100029 China.
[5]College of Earth and Planetary Sciences, University of Chinese Academy of Sciences, Beijing, 100029 China.

*Correspondence to*: Yong Wang (yongw@mail.tsinghua.edu.cn)

**Abstract.** All current global climate models (GCMs) only utilize grid-averaged surface heat fluxes to drive the atmosphere,
15  and thus, their subgrid horizontal variations and partitioning are absent. This can result in many simulation biases. To address this shortcoming, a novel parameterization scheme considering the subgrid variations of the sensible and latent heat fluxes to the atmosphere and the associated partitioning is developed and implemented into the National Center for Atmospheric Research (NCAR) Climate Earth System Model 1.2 (CESM1.2). The evaluations show that in addition to the improved boreal summer precipitation simulation over eastern China and the coastal areas of the Bay of Bengal, the longstanding
20  overestimations of precipitation on the southern and eastern margins of the Tibetan Plateau (TP) in most GCMs are significantly mitigated. The improved precipitation simulation on the southern and eastern margins of the TP is from suppressed large-scale precipitation. Moisture advection for precipitation production is blocked toward the southern edge of the TP, and the intensity of the moisture transport to the eastern edge is weakened. The corrected large-scale circulation in the lower atmosphere due to the realistic simulations of the grid-scale surface radiative and heat fluxes is responsible for the change
25  in moisture transport. In terms of global annual mean states, some improvements are obtained by the new scheme compared to the default CESM1.2 and the scheme stochastically allocating the subgrid surface heat fluxes to the atmosphere (i.e., without subgrid partitioning included). This study highlights the importance of subgrid surface energy variations and partitioning to the atmosphere in the simulation of the hydrological and energy cycles in GCMs.

## 1 Introduction

30  The importance of land surface heterogeneity has been proven through many observational and modeling studies (e.g., Taylor et al., 2007; Lothon et al., 2011; Rochetin et al., 2017; Wang et al., 2017). The variability of the surface heat fluxes caused by

the heterogeneity of the surface properties is crucial to the turbulence in the planetary boundary layer (PBL), as well as the evolution of large-scale atmospheric circulation and clouds (Rieck et al., 2014; Lee et al., 2019). In most global climate models (GCMs), confined by the horizontal resolution (~100–200 km), the subgrid surface heat fluxes to the atmosphere are averaged

35 out, thus degrading the simulation of convection and PBL processes. This results in most of the precipitation simulation errors in GCMs, such as the bias of the rainfall intensity spectrum (e.g., Wang et al., 2021a) and the unrealistic precipitation over the Indian summer monsoon region (e.g., Waliser et al., 2012; Wang et al., 2018) and the eastern and southern parts of the steep Tibetan Plateau (TP) (e.g., Zhou et al., 2021).

The land surface energy balance involves many biophysical and biogeochemical processes (Lee et al., 2011; Liu et al., 2014;

40 Duveiller et al., 2018; Chakraborty and Lee, 2019), which are closely related to surface properties. For instance, forests dissipate sensible heat to the PBL more efficiently than open landscapes (Rotenberg and Yakir, 2010; Wei et al., 2021), and changes in vegetation density have been found to favor the release of latent heat rather than sensible heat during the past three and a half decades (Forzieri et al., 2020). The different performance of the energy terms also suggests the potential importance of surface energy partitioning. However, the grid-scale surface heat fluxes to the atmosphere are rudimentarily treated by

45 calculating the weighted averages within each grid cell in all GCMs. This simplified approach inevitably hampers our understanding of the realistic small-scale land-atmosphere feedback, which is among the critical processes in the efforts to predict future climate change through GCMs (Miralles et al., 2019; Forzieri et al., 2020).

To incorporate the subgrid horizontal variations in the surface heat fluxes to the atmosphere resulting from land cover heterogeneity, a recent study (Sun et al., 2021) proposed a parameterization using stochastic sampling and tested it in the

50 National Center for Atmospheric Research (NCAR) Climate Earth System Model 1.2 (CESM1.2). It was found that this scheme improved the boreal summer precipitation simulation over eastern China. However, Sun et al. (2021) did not comprehensively assess the performance of other variables, and another important limitation is that the simulated summer precipitation on the southern and eastern margins of the TP, similar to most GCMs, is still overestimated compared to observations.

55 The simulation of the TP, which plays an important role in controlling the Asian and global climate, is a longstanding challenge for all of the current GCMs (Mueller and Seneviratne, 2014; Ma et al., 2015). These difficulties arise from the heterogeneity of the underlying surface, the complex terrain, and the sparse observation data used for constraints (Zhou et al., 2019; Liu et al., 2021). All of these factors make it difficult for the existing parameterization schemes to accurately reproduce complex subgrid-scale processes, resulting in degradation of the simulation in the TP region.

60 In the Sun et al. (2021) scheme, although the subgrid surface heat fluxes to the atmosphere are parameterized via stochastic sampling and internally multiple calls of the PBL and convection schemes, the underlying relationship between the subgrid heat fluxes is neglected. The conversion of the surface available energy into latent and sensible heat fluxes on a subgrid scale exerts a strong control on global water and energy cycles (Pitman, 2003; Tang et al., 2014; Wang et al., 2021b) by regulating land-atmosphere feedback, especially in regions with complicated land surface features, such as the TP and its surrounding

65 areas (Pielke et al., 2001; Findell et al., 2011; Forzieri et al., 2018, 2020). As the next logical step, in this study, the Sun et al.

(2021) parameterization is updated by taking the partitioning between the subgrid sensible and latent heat fluxes into account to better reproduce the variations in the subgrid land surface heat fluxes. It is highly desirable to alleviate the precipitation simulation biases in the TP region through this modification. Given that only the simulated precipitation by the Sun et al. (2021) scheme was investigated, its performance on the simulations of other variables such as grid scale surface heat fluxes, 2 m air

70 temperature and clouds is evaluated thoroughly in this study along with that in the modified parameterization.

The manuscript is organized as follows. Section 2 briefly describes the Sun et al. (2021) parameterization scheme and the modifications, CESM and experiments, and the observation and reanalysis datasets. The evaluations of the two schemes based on observations and reanalyses are presented in Sect. 3. The uncertainties are discussed in Sect. 4, while the conclusions are given in Sect. 5.

## 75  2 Parameterizations, CESM, Experiments, and Observations

### 2.1 CESM and Subgrid Heat Flux Scheme

The GCM used in this study is the NCAR CESM1.2, which is a state-of-the-art global coupled climate model. The atmospheric component is the Community Atmosphere Model, version 5 (CAM5). The land model is the Community Land Model, version 4 (CLM4). The spatial land surface heterogeneity in the default CLM4 is represented as a nested subgrid hierarchy in which

80 the grid cells are composed of multiple land units, snow/soil columns, and plant functional types (PFTs) (Oleson et al., 2010). All of the fluxes to and from the surface, including the heat fluxes, are defined at the PFT level. Since the subgrid heat fluxes exported to the CAM5 are weighted averages and their weights depend on the PFT area relative to all of the PFTs in the grid cell, the subgrid variations in the land surface fluxes are missing during the land-atmosphere coupling process (Sun et al., 2021).

85 To consider the influences of the heterogeneity of the subgrid heat fluxes to the atmosphere in CESM1.2, a parameterization scheme was developed and implemented in CLM4. This scheme established the statistical distributions of the subgrid sensible and latent heat fluxes within one grid cell. $N$ (i.e., the maximum number of PFTs ever coexisting in the grid cell) samples of sensible heat fluxes and $N$ samples of latent heat fluxes were independently and randomly selected as $N$ pairs to drive $N$ independent groups of the PBL and the deep convection parameterization schemes in CAM5. The outputs from these $N$ calls

90 of the schemes were then averaged with equal weights as the inputs of the other schemes. The stochastic sampling implicitly parameterized the uncertainties of the PBL and convection processes to a certain degree. As stated in Sun et al. (2021), using the sampled fluxes from a statistical distribution rather than the fluxes directly from individual PFTs can represent the mix of subgrid fluxes from horizontally mixed land cover types in reality. The Sun et al. (2021) scheme is very flexible and can be conveniently applied in different GCMs. For more details, refer to Sun et al. (2021).

## 2.2 Modified Subgrid Heat Flux Scheme

95

In the stochastic scheme proposed by Sun et al. (2021), the subgrid sensible heat and latent heat fluxes were individually and randomly selected from their normal distributions, without considering the underlying relationship between these two energy terms. However, we can compute the correlation coefficients between the subgrid sensible and latent heat fluxes within each grid cell using the following equation:

100
$$r = \frac{\sum_{i=1}^{n} w_i (F_{SH_i} - \bar{F}_{SH})(F_{LH_i} - \bar{F}_{LH})}{\sigma_{SH} \sigma_{LH}} \tag{1}$$

where $n$ is the number of PFTs within a grid cell in the land model; $w_i$ is the area percentage of each PFT within the grid cell; $F_{SH_i}$ and $F_{LH_i}$ are the subgrid surface sensible and latent heat fluxes of each PFT, respectively; $\bar{F}_{SH}$ and $\bar{F}_{LH}$ are the weighted averages of the subgrid sensible and latent heat fluxes in one grid cell, respectively; and $\sigma_{SH}$ and $\sigma_{LH}$ are the standard deviations of the subgrid sensible and latent heat fluxes in one grid cell, respectively, the calculation formulas of which are given in Sun

105  et al. (2021). Figure 1 shows that the energy partitioning between the sensible heat and latent heat fluxes at the subgrid scale is prominent. There are negative correlations at low latitudes in the Northern Hemisphere (NH) and most of the Southern Hemisphere (SH), whereas in the middle and high latitude regions in the NH and on the TP, most of the regions have positive correlations. A possible explanation for these positive correlations is that in these regions, snow melting usually occurs, leading to larger subgrid sensible heat flux from enhanced surface net radiation due to reduced snow albedo. Thus, during this period,

110  the land surface gains more water for evaporation (i.e., latent heat flux).
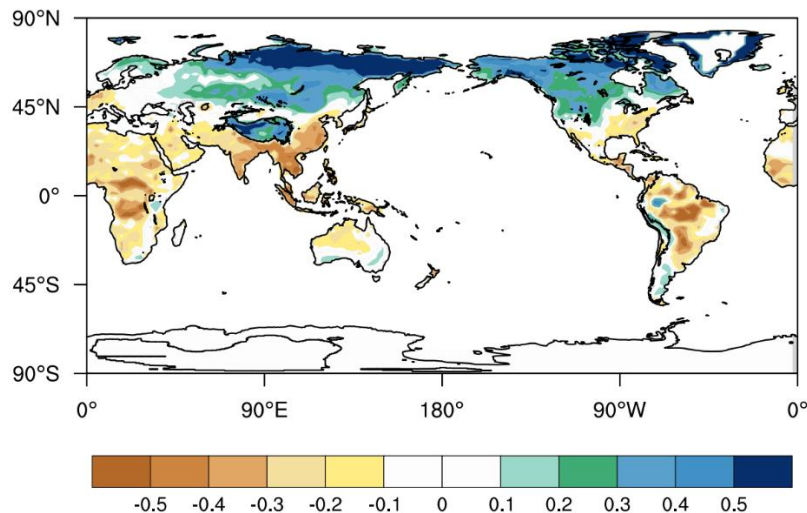


**Figure 1: Spatial distribution of the annual mean correlation coefficient *r* between the subgrid surface sensible heat and latent heat fluxes in the EXP_COR simulation.**

Based on the notion that subgrid energy partitioning between the surface and the PBL is important in the land-atmosphere

115  coupling process, several improvements are made to the Sun et al. (2021) scheme in this study. Two simplified methods are developed.

(1) Arrange the randomly selected $N$ subgrid sensible heat (SH) fluxes and $N$ subgrid latent heat (LH) fluxes in each grid cell from largest to smallest and use the $N$ pairs of matching sensible and latent heat fluxes to drive the atmosphere independently. That is, a large (small) SH flux corresponds to a large (small) SH flux.

120 (2) Arrange the randomly selected $N$ subgrid sensible heat fluxes from largest to smallest and arrange the $N$ latent heat fluxes from smallest to largest in each grid cell. Then, the $N$ pairs of matching sensible and latent heat fluxes are used to drive the atmosphere independently. That is, a large (small) subgrid SH flux corresponds to a small (large) subgrid LH flux.

Which one is used for a given grid cell depends on the time varying correlation coefficient $r$. If the correlation coefficient $r$ in the grid cell is positive, the PBL and convection parameterizations are driven using the heat fluxes derived in method one.

125 Otherwise, the heat fluxes selected using method two will be passed to the atmosphere. The arithmetic mean of the outputs from $N$ calls of the PBL and the convection parameterizations is input into the other following schemes.

## 2.3 Experiments

Three Atmospheric Model Intercomparison Project (AMIP)-type experiments with a finite volume dynamical core at a horizontal resolution of 1.9°×2.5° (~2°) and 30 vertical levels from the surface to 3.6 hPa were conducted using observed

130 climatological (1982–2001 mean) monthly sea surface temperature and sea ice extent data (Stone et al., 2018). One control simulation (CTL) uses the standard CESM1.2, another experimental simulation (EXP) uses the Sun et al. (2021) parameterization in CESM1.2 (also the same as the EXP run in their study), and the third improves the EXP run using the modifications described in Sect. 2.2 (EXP_COR). All of the simulations were run for six years, with the first year discarded as the spin-up stage. The value of $N$ in each grid was fixed to 16, which equals the maximum number of PFTs ever coexisting

135 on a single column in the land model, although different grid cells have different numbers of PFTs (Sun et al., 2021). As noted in Sun et al. (2021), further increasing $N$ has negligible impacts on the model performance compared to setting $N$ to 16 and enhances computational loading instead.

## 2.4 Observations and Reanalyses

To evaluate the model performance, the simulation results are compared with the available observation and reanalysis datasets.

140 The Tropical Rainfall Measuring Mission (TRMM; Huffman et al., 2014) observations (0.25°×0.25°) and the Modern-Era Retrospective Analysis for Research and Applications, Version 2 (MERRA-2; Gelaro et al., 2017) reanalysis (0.5°×0.625°) are used for precipitation. The other datasets include surface radiative fluxes from the Clouds and the Earth's Radiation Energy Systems (CERES) Energy Balanced and Filled (1.0°×1.0°) (EBAF; Loeb et al., 2012), sensible heat and latent heat fluxes from the Global Land Data Assimilation System Version 2.1 (GLDAS-2.1) Noah monthly data (1.0°×1.0°) (Rodell et al., 2004) and

145 2 m air temperature from the Climatic Research Unit with a 0.5° resolution (CRU; Harris et al., 2020). For consistency, all of the observation/reanalysis datasets are regridded to the same grid size as CAM5.

## 3 Results

Sun et al. (2021) found that the improved precipitation simulation with the parameterization of subgrid surface heat fluxes to the atmosphere is most prominent for boreal summer and in Asia. In this regard, the following analyses are also focused on

150    Asian summer. Note that the global annual statistics are still evaluated and presented in Sect. 3.3.

### 3.1 Precipitation

Sun et al. (2021) (the EXP run) improved the simulation of the summer precipitation over eastern China and the coastal areas of the Bay of Bengal (Fig. 2c), which was attributed to altered vertical diffusion and convection. However, it still produces overestimations on the eastern and southern margins of the TP (Fig. 2d). It is encouraging that after taking the subgrid energy

155    partitioning into account, the longstanding biases are efficiently mitigated in the EXP_COR run (Fig. 2e). Among the three simulations, the EXP_COR run is closest to the observations. The regionally averaged root mean square error (RMSE) decreases from 3.11 in the CTL run and 2.91 in the EXP run to 2.88 in the EXP_COR run, and the spatial correlation coefficient (COR) increases from 0.65 in the CTL run to 0.7 in the EXP and EXP_COR runs.
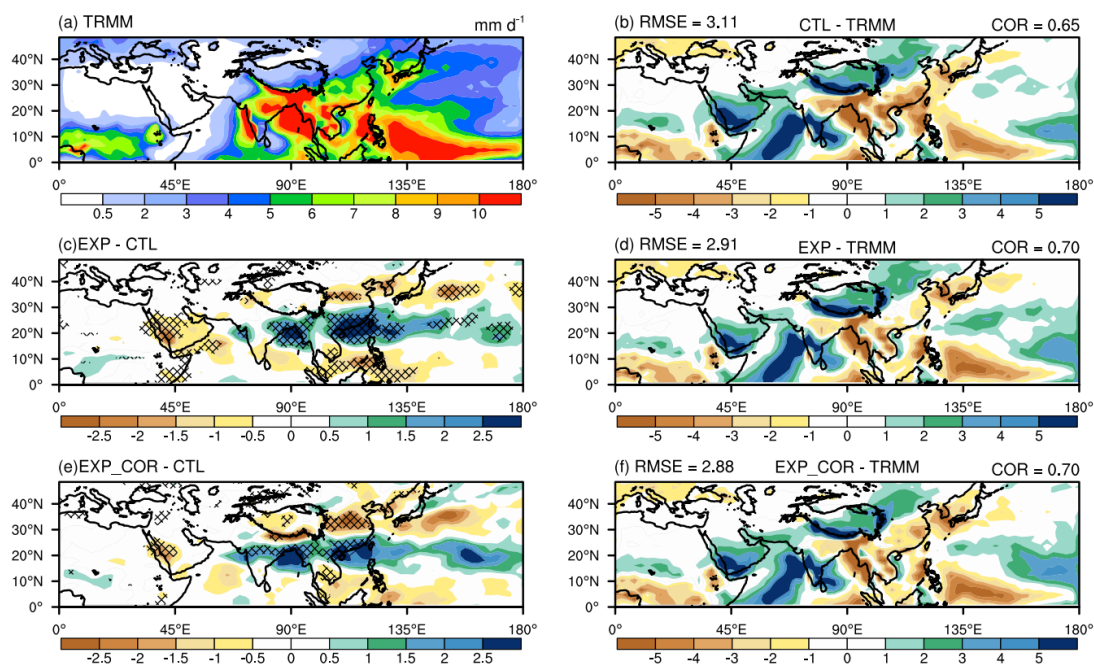


160    **Figure 2: Spatial distributions of the JJA (June-July August) mean precipitation for (a) TRMM, the biases of (b) CTL, (d) EXP, and (f) EXP_COR with respect to TRMM, and the differences between EXP and CTL (c) and between EXP_COR and CTL (e). The crossed areas are significant at the 95% level.**

The total precipitation in the model consists of convective and large-scale precipitation. We zoom in on the southern and eastern edges of the TP with improvements in the EXP_COR run to see their contributions (Fig. 3). Figures 3a&c show that

165    in the EXP run, compared to the CTL run, both large-scale precipitation and convective precipitation increase on the southern

border of the TP. On the eastern border of the TP, large-scale precipitation increases, and convective precipitation decreases. In contrast, in the EXP_COR run, large-scale precipitation is significantly suppressed on the southern fringe, and both large-scale precipitation and convective precipitation are reduced on the eastern margin.
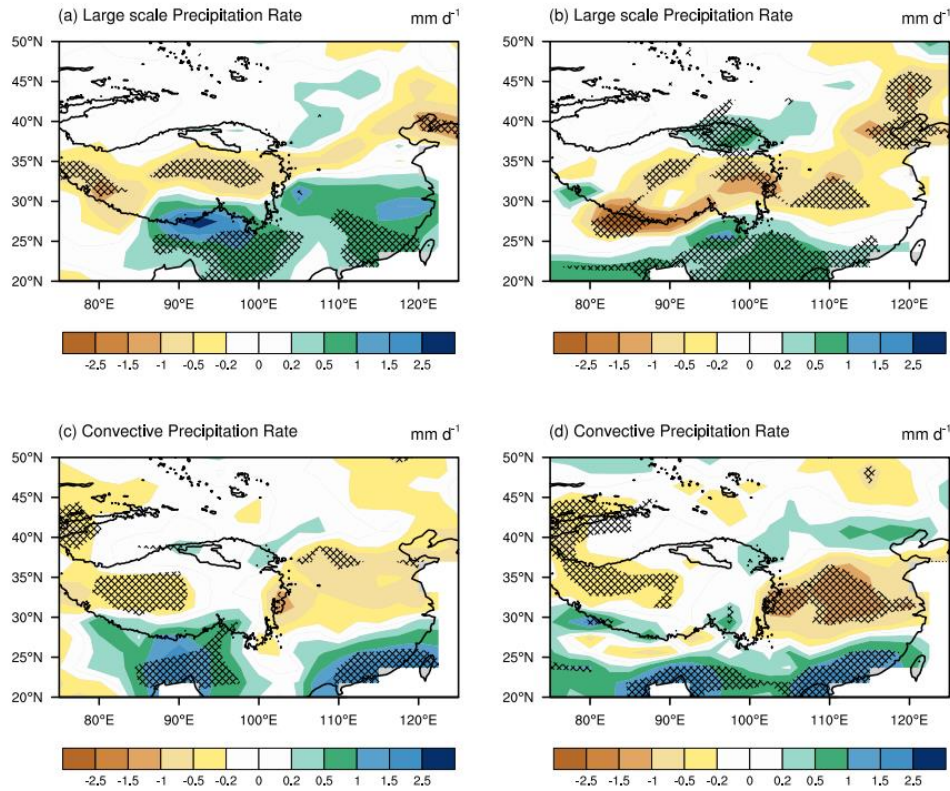


**Figure 3: Spatial distribution of the differences in (the first row) large-scale precipitation and (the second row) convective precipitation between (left) EXP and CTL and between (right) EXP_COR and CTL. The crossed areas are significant at the 95% level.**

A moisture budget analysis widely used in previous studies (Gao et al., 2017; Wang et al., 2016) is conducted to examine the causes of the precipitation changes. Following Sun et al. (2021), the atmospheric water vapor budget equation is given below:

$$\frac{\partial W}{\partial t} = \left(-W\nabla \cdot \vec{V}\right) + \left(-\vec{V} \cdot \nabla W\right) - P + E \tag{2}$$

where $P$ is precipitation and $E$ is evaporation. $W$ is the column integrated moisture given by $\int_{P_{top}}^{P_{bot}} qdp/g$, in which $q$ is the specific humidity, $P_{top}$ and $P_{bot}$ are the top and surface pressures, respectively, and $g$ is the acceleration due to gravity. The vector $\vec{V}$, given by $W^{-1} \int_{P_{top}}^{P_{bot}} (q\vec{u})dp/g$, represents the total horizontal moisture transport normalized to the column integrated moisture, where $\vec{u}$ is the horizontal wind vector. The first term on the right-hand side of Eq. (2) is the moisture convergence $Q_{cnvg}$, and the second term is the moisture advection $Q_{advt}$. The tendency of the term $\frac{\partial W}{\partial t}$ on the left-hand side of Eq. (2) is negligible for seasonal averages of multiple years.

Compared to the CTL run, moisture convergence weakens on the eastern edge of the TP, while moisture advection increases in the EXP_COR run (Figs. 4a&b). On the southern edge of the TP, moisture advection decreases, and moisture convergence slightly increases. Overall, the total water vapor contributions decrease on the eastern and southern edges of the TP (Fig. 4d).

185 We note that the spatial pattern of $Q_{cnvg}$, changes in the EXP_COR run relative to the CTL run, resembles that in the EXP run (Figs 4d&f in Sun et al., 2021), which is linked with the changes in the heating rate due to vertical diffusion in the PBL caused by the subgrid variations in land surface heat fluxes. In comparison with the EXP run, the negative moisture convergence anomaly is further aggravated, and the positive bias of moisture advection on the eastern margin of the TP is smaller (Sun et al. 2021). The negative maximum of the total contribution thus shifts westward to the eastern margin of the TP. On the southern

190 edge of the TP, the main term contributing to precipitation changes is due to the reduced moisture advection (Fig. 4b).
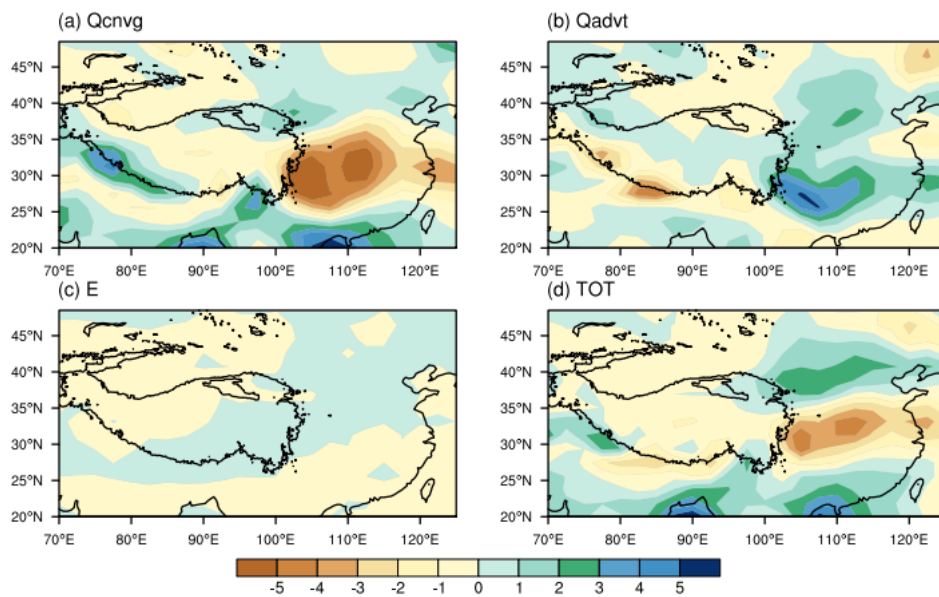


Figure 4: Spatial distributions of JJA mean differences in (a) moisture convergence $Q_{cnvg}$, (b) moisture advection $Q_{advt}$, (c) evaporation $E$, and (d) the total contribution $Q_{cnvg} + Q_{advt} + E$ between the EXP_COR and CTL runs.

The changes in associated atmospheric circulation and moisture transport are illustrated in Fig. 5, where the MERRA-2
195 reanalysis is used for comparison with the model simulations. A large amount of water vapor from the Bay of Bengal is transported to the southern margin of the TP, resulting in heavy rainfall on the southern slope of the TP (Fig. 5a). Compared to MERRA-2, the sea level pressure (SLP) on the TP in the CTL run is overestimated (Fig. 5c). In the EXP run (Fig. 5b in Sun et al., 2021), the sea level pressure decreases on the TP compared to the CTL run. However, a relatively strong negative anomaly occurs along the Bay of Bengal, inducing cyclonic moisture transport from the ocean. This abnormal circulation

200 transports excessive moisture to the southern edge of the TP, causing the overestimation of the rainfall in this area. In contrast, in the EXP_COR run (Fig. 5d), the SLP simulation is corrected, and the anomalous east–west pressure gradient along 30° N results in an easterly anomaly on the southern margin of the TP, which blocks moisture transport from the ocean in the south. On the eastern margin of the TP, compared to Fig. 5b in Sun et al. (2021), the anomalous zonal pressure gradient in the

midlatitude region is weakened in the EXP_COR run (Fig. 5d). The weakened pressure anomalies cause moisture advection

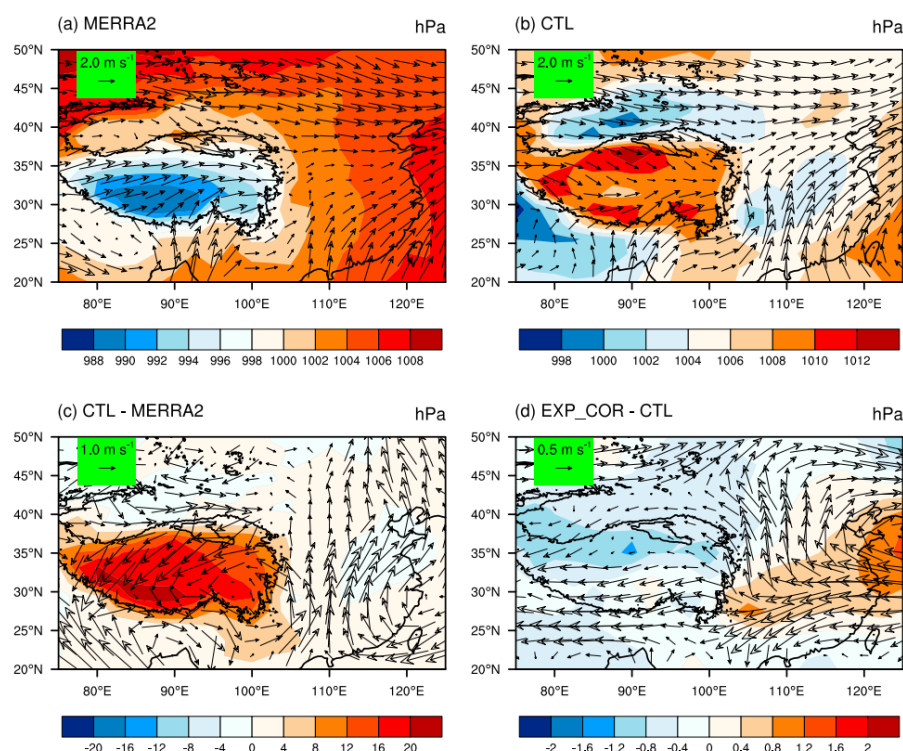205 from the ocean in the east to weaken and decrease the rainfall on the eastern border of the TP.
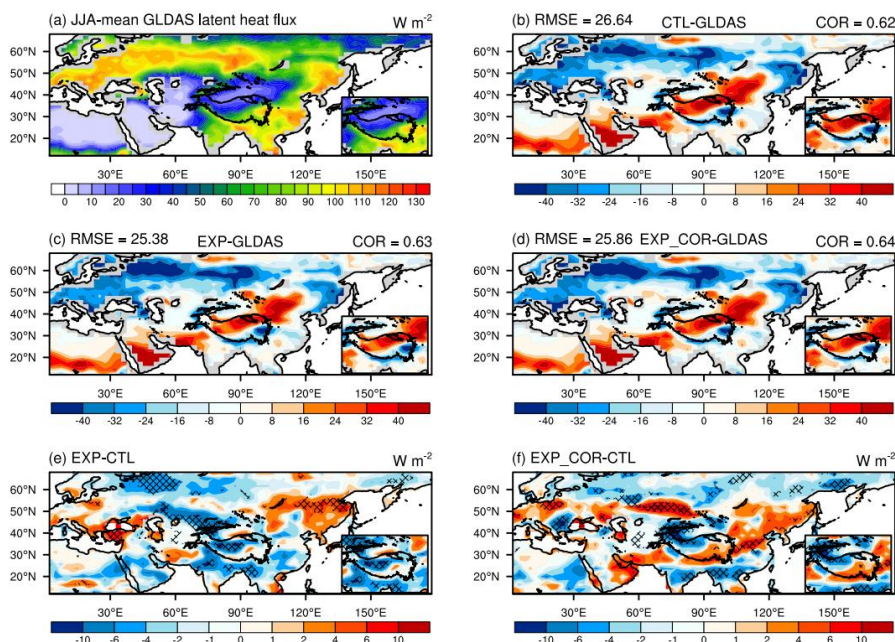


**Figure 5: Spatial distributions of the JJA mean SLP superposed by the moisture transport vector $\vec{V}$ from (a) MERRA-2 and (b) CTL. The differences in the SLP superposed by the anomalies of moisture transport vector $\vec{V}$ between (c) CTL and MERRA-2 and (d) EXP_COR and CTL.**

210 **3.2 Surface Heat Fluxes, 2 m Air Temperature and Clouds**

The above analysis indicates that the precipitation simulation is improved through the correction of large-scale atmospheric circulation in the lower atmosphere, which is highly linked with grid-scale surface heating/cooling. It will be illustrated below that this improvement is due to the changes in the simulated surface energy budget and 2 m air temperature. The evaluations of the latent heat flux simulation are shown in Fig. 6. Compared to the CTL run, the EXP run increases the latent heat fluxes

215 over northeastern China and southeastern Russia (Fig. 6e). It also decreases the latent heat fluxes over southern China, the northwestern TP, and along the Bay of Bengal. In the EXP_COR run, the decreased latent heat fluxes on the northwestern TP still exist, and the underestimations on the southern and eastern margins of the TP in the CTL run are remarkably improved (Fig. 6f). In the EXP run, the sensible heat fluxes are stronger over northern China, the TP, and southeastern Russia and are weaker over southern China compared to the CTL run (Fig. 7e). The sensible heat flux changes in the EXP_COR run are more

220 significant than those in the EXP run (Fig. 7f), especially over northern China and the southern and eastern margins of the TP, resulting in better agreement with the observations.

**Figure 6: Spatial distributions of the JJA mean latent heat flux in (a) GLDAS (upward positive), the biases of (b) CTL, (c) EXP, and (d) EXP_COR with respect to the GLDAS data, and the differences between (e) EXP and CTL and between (f) EXP_COR and CTL.**
225 **The crossed areas are significant at the 95% level. The boxes in the bottom right corner show the conditions on the TP, where the regionally averaged spatial correlation coefficient (COR) and root mean square error (RMSE) are calculated.**
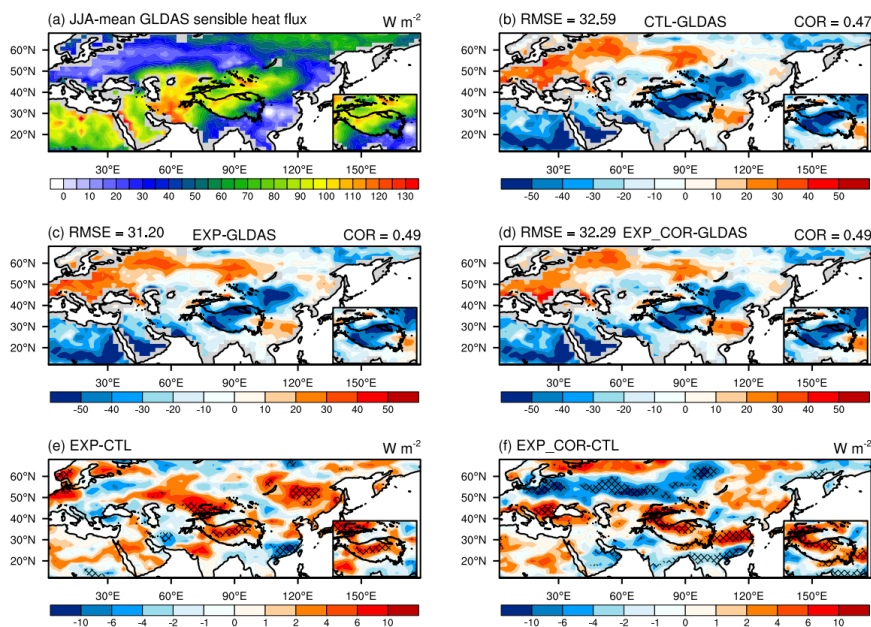


**Figure 7: Spatial distributions of the JJA mean sensible heat flux in (a) GLDAS (upward positive), the biases of (b) CTL, (c) EXP, and (d) EXP_COR with respect to GLDAS, and the differences between (e) EXP and CTL and between (f) EXP_COR and CTL.**
230 **The crossed areas are significant at the 95% level. The boxes in the bottom right corner show the conditions on the TP, where the regionally averaged COR and RMSE are calculated.**

The spatial distribution of JJA mean 2 m air temperature from CRU and the difference between the observations and the three experiments are shown in Fig. 8. Compared to the CTL run, the 2 m air temperature over southern China is lower in the EXP run and fits the observations better. However, over northeastern China and southeastern Russia, the simulation is not significantly improved. In contrast, in the EXP_COR run, the 2 m temperatures over northern China, northeastern China, and the TP are dramatically increased. In addition, over the northern part of the Eurasian continent, the overestimation of the 2 m temperature in the CTL run is also alleviated to some extent. Overall, the changes in the EXP_COR run relative to the CTL run resemble those of the sensible heat flux (Fig. 7). This implies that the change in the surface sensible heat flux regulates the change in 2 m air temperature via the multiple calls of the PBL and convection schemes at the subgrid scale (Sun et al., 2021) and the atmospheric feedback at the grid scale.
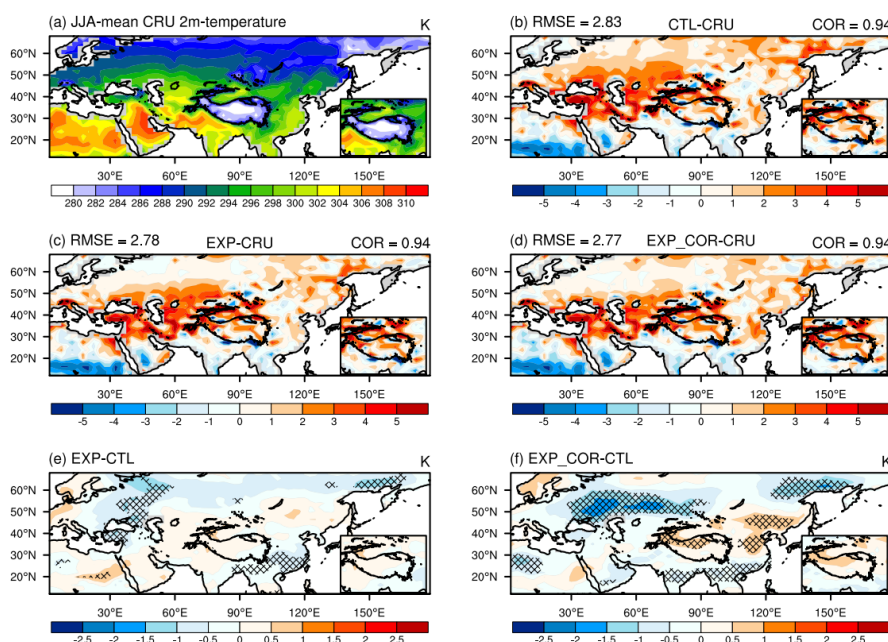


Figure 8: Spatial distributions of the JJA mean 2 m temperature in (a) the CRU, the biases of (b) CTL, (c) EXP, and (d) EXP_COR with respect to CRU, and the differences between (e) EXP and CTL and between (f) EXP_COR and CTL. The crossed areas are significant at the 95% level. The boxes in the bottom right corner show the conditions on the TP, where the regionally averaged COR and RMSE are calculated.

At the grid scale, after receiving shortwave radiation, in addition to emitting longwave radiation into the atmosphere, the land surface transports energy upward in the form of sensible and latent heat fluxes. Therefore, the adjustment of the surface heat fluxes is regulated by the simulation of the surface radiation (Fig. 9). The JJA mean net surface shortwave flux measured by CERES-EBAF is positive (downward positive) (Fig. 9a). Compared to CERES-EBAF, the CTL run receives more net shortwave flux over southern China, and it gains less over almost all of the rest of China and southeastern Russia (Fig. 9b). The underestimation on the TP and the overestimation over southern China are alleviated in the EXP run (Fig. 9e). In the EXP_COR run, in addition to the already existing significant improvements in the EXP run, the net surface shortwave fluxes

over northern China and on the southern and eastern margins of the TP are markedly increased, agreeing better with the observations. The simulated patterns of the net surface shortwave and longwave fluxes (upward positive) are essentially

255 consistent (figure not shown). The more (less) shortwave radiation is received by the surface, the more (less) heat it directly obtains, and the more (less) sensible heat flux it emits to warm (cool) the atmosphere.
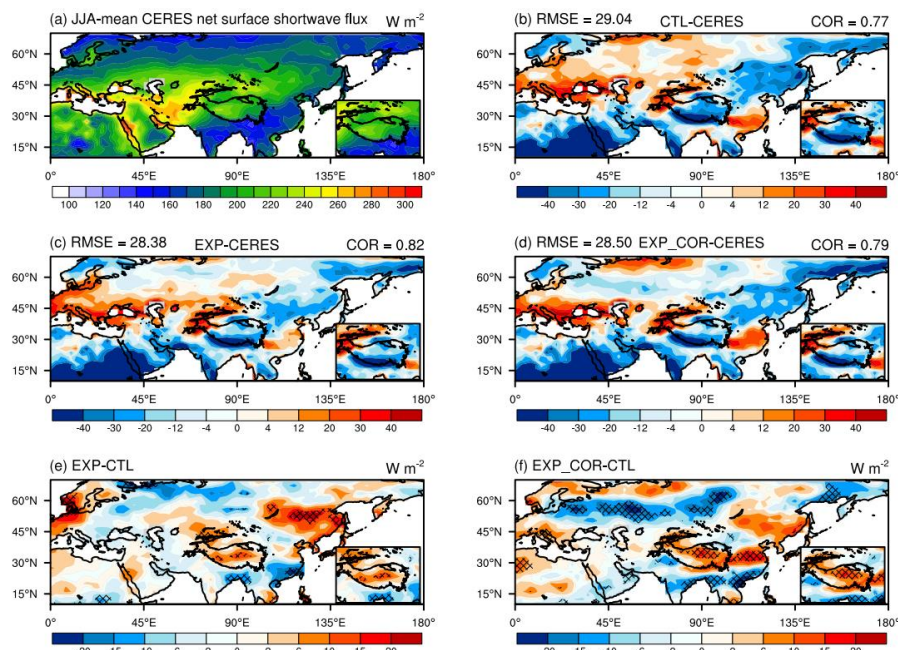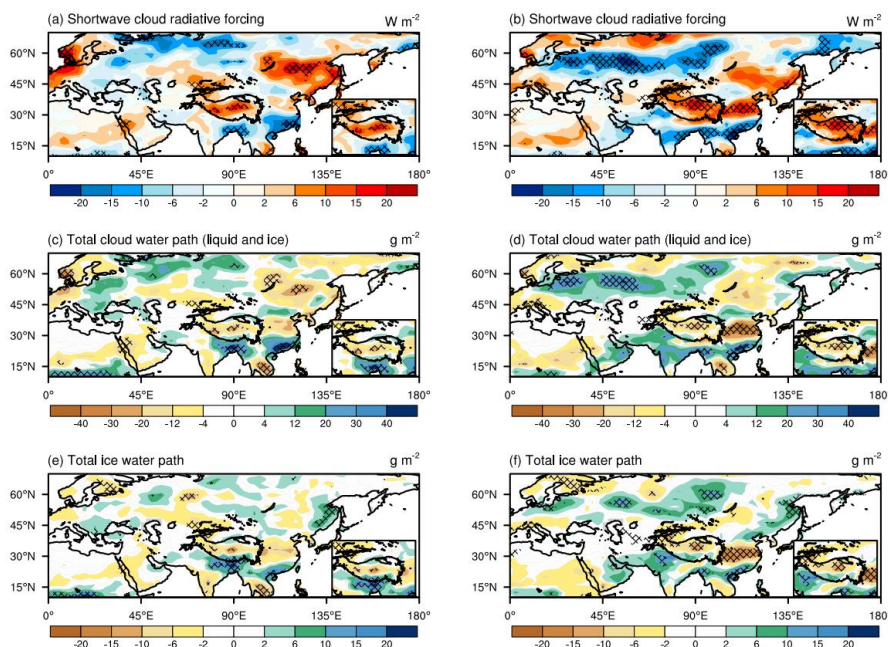


**Figure 9: Spatial distributions of the JJA mean net surface shortwave flux in (a) CERES-EBAF (downward positive), the biases of (b) CTL, (c) EXP, and (d) EXP_COR with respect to CERES-EBAF, and the differences between (e) EXP and CTL and between (f)**
260 **EXP_COR and CTL. The crossed areas are significant at the 95% level. The boxes in the bottom right corner show the conditions on the TP, where the regionally averaged COR and RMSE are calculated.**

Since clouds have a significant radiative effect (Sohn, 1999), they are investigated. Generally, the radiative effect of clouds is quantified by cloud radiative forcing (CRF) (the difference in the surface net flux between all sky and clear sky conditions). It includes shortwave cloud forcing (SWCF) and longwave cloud forcing (LWCF). Realistic simulation of the CRF is another

265 important measure of the performance of climate models (Sun et al., 2016). The SWCF is negative, and a smaller value indicates a stronger reflection of the solar shortwave radiation. Fig. 10a demonstrates that in the EXP run, SWCF is weakened over northeastern China, the TP, and southeastern Russia and is enhanced over southern China and along the Bay of Bengal compared to the CTL run. In the EXP_COR run, the reductions over northern China and the TP are more significant, which means that less radiation is reflected by clouds. It should be noted that there is a significant negative band along 60°N. The

270 LWCFs are positive, and a larger value means a stronger warming effect on the land surface. The LWCFs increase over southern China and decrease over northern China (figure not shown). The distribution of the net CRF (figure not shown) resembles that of the SWCF, which implies that the SWCF is dominant in the CRF variations in these regions. The distribution

of SWCF (Figs. 10a&b) is very consistent with that of the net surface shortwave flux (Figs. 9e&f), implying that the net surface radiation fluxes are mainly dominated by the shortwave radiation reflected by clouds.



275

**Figure 10: Spatial distributions of the differences in shortwave cloud radiative forcing (the first row, units: W m$^{-2}$), total cloud water path (the second row, units: g m$^{-2}$), and total ice water path (the third row, units: g m$^{-2}$) between EXP and CTL (left) and between EXP_COR and CTL (right). The crossed areas are significant at the 95% level. The boxes in the bottom right corner show the conditions on the TP.**

280 The cloud properties affecting the cloud radiative effects include their macrostructures (e.g., fraction, top and base heights, and vertical overlap) and microphysical properties (e.g., particle size distribution and geometric configuration, cloud phase and water condensation). The simulations of the total cloud water path (vertically integrated cloud liquid and ice water content) are shown in Figs. 10c&d. A higher cloud water content reflects more solar radiation. The EXP run increases the total cloud water path over southern China and decreases that over northeastern China, the TP, and southeastern Russia. The spatial

285 distribution of the total ice water path is consistent with that of the total cloud water path. With the modified scheme, the EXP_COR run enhances the respective changes over northeastern and southeastern China, consistent with the changes in SWCF.

As shown in Fig. 11, after introducing the modified parameterization (EXP_COR) into CESM1.2, the low cloud fraction over northern China and southeastern Russia is reduced, while low clouds are increased significantly over southern China in

290 comparison with the CTL run. The EXP run has a similar pattern of changes but with smaller magnitudes compared with the EXP_COR run. Low clouds reflect a larger amount of incoming solar radiation and emit longwave radiation at relatively high temperatures, so they exert an overall net cooling effect on the Earth (Klein and Hartmann, 1993; Hartmann, 1994). Compared to the CTL run, the middle and high clouds on the TP are dramatically decreased in the EXP_COR run, and the land surface

is warmed because it gains more net solar radiation. Especially for high clouds, the decrease in the EXP_COR run is much

295   larger than that in the EXP run. Overall, both the cloud fraction and the cloud water path simulations indicate that on the TP,

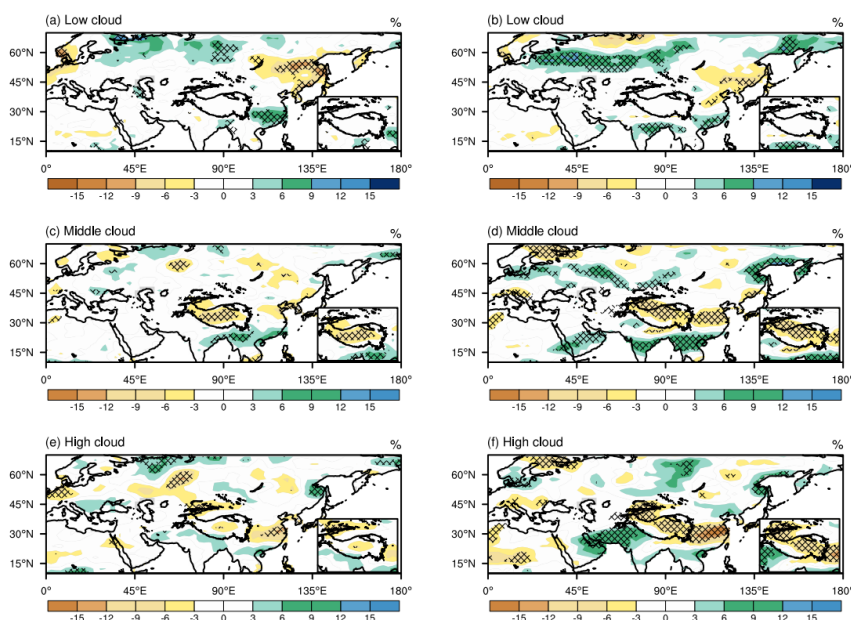the net solar radiation received by the land surface is increased in the EXP_COR run.



**Figure 11: Same as Figure 10 but for (a) & (b) low, (c) & (d) middle, and (e) & (f) high clouds. The crossed areas are significant at the 95% level. The boxes in the bottom right corner show the conditions on the TP.**

## 3.3 Mean States

The analyses presented above demonstrate that the introduction of the modified parameterization scheme (EXP_COR), compared to the default model, significantly improves the simulations of summer precipitation in Asia along with the changes in simulated surface heat fluxes, 2 m air temperature and cloud properties. The precipitation improvements over eastern China are mainly from the consideration of subgrid variations in surface heat fluxes (EXP), while those on the southern and eastern

305   margins of the TP are attributed to their subgrid partitioning. An overall evaluation of the global annual mean states is also necessary because from the perspective of climate model development, the incorporation of a new parameterization scheme to improve some aspects should not cause degradation of other aspects (Wang et al., 2021b). A summary of the various statistics of the three experiments (CTL, EXP, and EXP_COR) using a Taylor diagram is presented in Fig. 12. The evaluation metrics used for the comparison are listed in the bottom left corner of the figure. Overall, all of the simulation statistics of the

310   EXP_COR run are comparable to those of the CTL run, and it outperforms the EXP run for some of the metrics. For instance, the EXP run has larger variations and small spatial correlations for the SLP, relative humidity, and temperature simulations than the EXP_COR and CTL runs. The degradation of humidity and temperature in the EXP run implies the necessity and importance of parameterizing the subgrid partitioning of land surface heat fluxes to the atmosphere in GCMs.

14
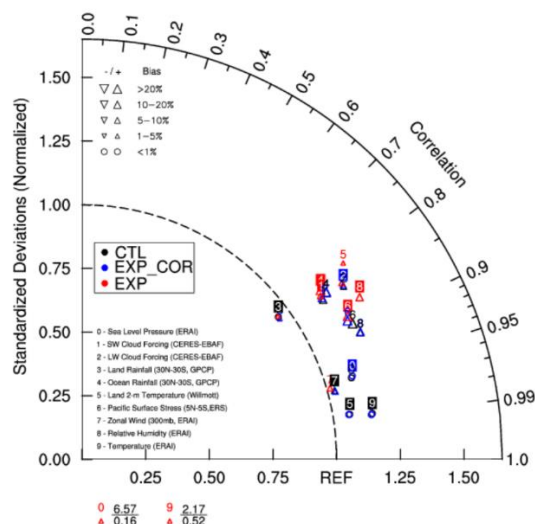
**Figure 12: Taylor diagram of the global annual mean metrics for CTL (black), EXP_COR (blue), and EXP (red). SW: shortwave; LW: longwave.**

The zonal means of the temperature and specific humidity from the European Centre for Medium-Range Weather Forecasts (ECMWF) ERA-Interim reanalysis dataset and the model biases are shown in Fig. 13. In the CTL run, the temperature is overestimated at lower levels in the tropics and midlatitude regions in the SH, whereas at other latitudes and levels, it is generally underestimated (Fig. 13a). The EXP run reverses the positive biases back to negative biases with an excessive reduction at lower levels, and the negative biases in other regions are further exacerbated (Fig. 13b). In contrast, the changes in the EXP_COR run are moderate. The low-latitude overestimations in the lower troposphere and the high-latitude underestimations across the troposphere are alleviated to some extent (Fig. 13c). In the simulation of the specific humidity, compared to the observations, the main positive biases occur in the low latitude and midlatitude regions below the middle troposphere (Fig. 13d). For the midlatitude region in the NH, there are negative biases at lower levels. In the EXP run, the positive biases are alleviated, but the negative biases are slightly increased (Fig. 13e). The values of the EXP_COR run are comparable to those of the CTL run, and their differences are minor and negligible from the perspective of the annual zonal averages (Fig. 13f). In summary, the performance of the mean state simulations does not change significantly when using the modified scheme (EXP_COR), indicating that the subgrid parameterization scheme can be incorporated into the GCMs without heavy retuning.
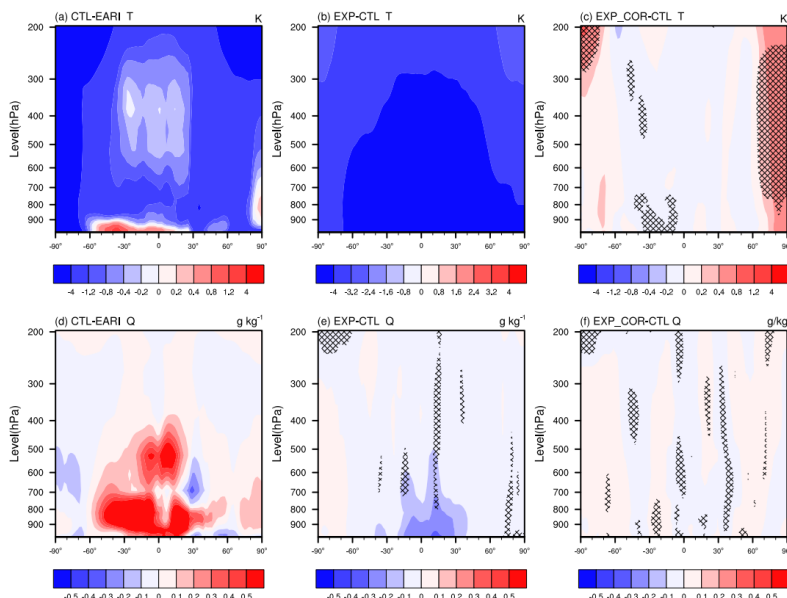
Geoscientific
Model Development
Discussions



**Figure 13:** Annual and zonal mean cross-sections of the (a–c) temperature and (d–f) specific humidity differences for (a, d) CTL-ERAI, (b, e) EXP-CTL, and (c, f) EXP_COR-CTL. The crossed areas are significant at the 95% level.

## 4 Discussion

335    Despite the uncertainties in the observations, the overestimated rainfall on the southern and eastern margins of the Tibetan Plateau in the GCMs is widely acknowledged when comparing multiple observations (Mehran et al., 2014; Yu et al., 2015). The uncertainties for the evaluations of other modeled variables are discussed below. The CERES-EBAF datasets provide long-term global Earth radiation budget records from the surface to the top of the atmosphere (TOA) together with the associated cloud and aerosol properties. Extensive validation has been conducted for both TOA and surface radiation in

340    CERES-EBAF using TOA consistency tests and direct comparisons of surface fluxes with ground-based measurements over both land and ocean (Loeb et al., 2007; Loeb et al., 2012). Although some weaknesses are noted (e.g., LW cloud radiative effects at the surface on the TP are overestimated due to poor sampling of clear sky scenes during the night), they are widely used for climate model evaluations (Loeb et al., 2018; Hinkelman et al., 2019), and this flaw does not affect the conclusions in this study. As for surface sensible and latent heat fluxes, there are few observations covering the whole TP. Instead, among

345    various reanalysis datasets, GLDAS has been evaluated and analyzed extensively (Novick et al., 2018; Sun et al., 2018; Laloyaux et al., 2016). For instance, Jiménez et al. (2011) conducted a global intercomparison of monthly mean land surface heat flux products, including space-based observations and reanalyses including GLDAS. They demonstrated that the spatial distributions related to the major climatic regimes and geographical features are well reproduced by GLDAS. With comprehensive validations, the GLDAS product has been widely used in evaluating model-based studies (Saha et al., 2014;

350    Xia et al., 2019) such as water resource management (Zaitchik et al., 2010), and drought monitoring and prediction (Hao et al.,

2016). The CRU gridded dataset for 2 m air temperature has undergone a series of technical validations, such as quality control of input data, comparisons between versions and with alternative datasets, and cross-validation of the interpolated anomalies (Osborn et al., 2017; Harris et al., 2020)..

355  In addition to subgrid variation and partitioning of surface heat fluxes, there are other factors that can impact the precipitation simulation on the TP. For instance, subgrid topographic effects have large effects on latent heat and sensible heat fluxes. It is found that parameterizing them in GCMs influences the simulated surface energy balance and boundary conditions, as well as precipitation on the TP (Lee et al., 2019; Hao et al., 2021a, b). Alternatively, the accurate representation of land cover types and soil properties is vital to the realistic simulation of surface radiative and heat fluxes and thus TP rainfall (Liu et al., 2021; Yue et al., 2021).

360  The GCM used to test the schemes is CESM1.2, in which the land model is CLM4. Similar to CLM4, CLM5 (CLM version 5) in CESM2 (CESM version 2) and other land surface models in the GCMs use the PFT structure as well. Additionally, the parameterization of subgrid heat fluxes proposed in this study is not dependent on the specific parameterizations of the PBL and convection processes. Therefore, it is conveniently applied to other GCMs.

## 5 Conclusions

365  In this study, a parameterization of the subgrid variation and partitioning of the land surface heat fluxes to the atmosphere was developed and implemented in the NCAR CESM1.2. The modification to the Sun et al. (2021) scheme is based on the fact that energy redistribution with complex climate impacts between the land surface and the PBL plays an essential part in the global and regional energy cycles (Liu et al., 2014; Chakraborty and Lee, 2019; Wei et al., 2021). Three experiments were conducted to evaluate the updated scheme (CTL, EXP, and EXP_COR). The precipitation improvements over eastern China derived

370  using the original scheme (EXP) still exist in the new scheme (EXP_COR). In addition, the stubborn overestimations of precipitation on the southern and eastern margins of the TP are significantly alleviated. The possible causes are illustrated by the water vapor and energy budgets analyses.

On the southern edge of the TP, the overestimated large-scale precipitation and convective precipitation in the EXP run are both suppressed after parameterizing the subgrid energy partitioning in the EXP_COR run. The weakened precipitation is due

375  to blocking moisture advection from the Bay of Bengal toward the southern slope of the TP. On the eastern edge of the TP, the improvement is mainly derived from the change in large-scale precipitation. The excessive moisture advection from the ocean in the east is reduced due to the weakened east–west pressure gradient. The altered large-scale atmospheric circulation results from the changes in grid-scale surface energy fluxes and 2 m air temperature. The simulated latent and sensible heat fluxes on the TP are altered partly by the increased surface net radiation fluxes that cause near-surface warming there. The

380  changes in surface net radiation fluxes are from the modified cloud properties (cloud fraction and cloud water content).

Based on the comparison of the global annual mean states, the EXP_COR run performs better than the EXP run, especially for the simulations of temperature and humidity. The mean states did not change much after the introduction of the new parameterization scheme, and thus, the new scheme can be implemented in the CESM without heavy retuning.

385 The Sun et al. (2021) scheme offers a novel method of parametrizing the subgrid heterogeneity of surface heat fluxes to the atmosphere in GCMs. As a further modification, the significance of the correlation coefficients between the subgrid-scale sensible and latent heat fluxes is taken into account for a more realistic interpretation of the energy exchange processes. The findings of these two studies highlight the importance of the energy variation and redistribution between the land surface and the lower atmosphere at the subgrid scale.

**Code and data availability**

390 The CESM1.2.1-CAM5.3 source code can be downloaded through the CESM official website https://www.cesm.ucar.edu/models/cesm1.2/cesm/doc/usersguide/x290.html#download_ccsm_code. The modified CESM code as well as the CAM5 output for all simulations in the study are provided in an open repository Zenodo (https://zenodo.org/record/6606418#.YpiHWKhBw2w). The TRMM data are available from https://gpm.nasa.gov/data/directory. The MERRA-2 data files are available from

395 https://disc.gsfc.nasa.gov/datasets/M2IMNPASM_5.12.4/summary?keywords=M2IMNPASM_5.12.4%20instM_3d_asm_N p and https://disc.gsfc.nasa.gov/datasets/M2TMNXFLX_5.12.4/summary?keywords=M2TMNXFLX_5.12.4%20tavgM_2d_flx_N x. The CERES EBAF data are available from https://climatedataguide.ucar.edu/climate-data/ceres-ebaf-clouds-and-earths-radiant-energy-systems-ceres-energy-balanced-and-filled. The GLDAS-2.1 data are available from

400 https://disc.gsfc.nasa.gov/datasets/GLDAS_NOAH10_M_2.1/summary?keywords=GLDAS. The CRU data are available from https://crudata.uea.ac.uk/cru/data/hrg/?_ga=2.162163900.162961233.1636977076-620633058.1635581908.

**Author contribution**

YW conceived the idea. WS developed the model code. WS conducted the model simulations. MY and YW performed the analysis. MY and YW interpreted the results and wrote the paper. All authors participated in the revision and editing of the

405 paper.

**Competing interests**

The authors declare that they have no conflicts of interest.

**Disclaimer**

Publisher's note: Copernicus Publications remains neutral with regard to jurisdictional claims in published maps and
410    institutional affiliations.

**References**

415    Chakraborty, T. and Lee, X.: Land Cover Regulates the Spatial Variability of Temperature Response to the Direct Radiative
Effect of Aerosols, Geophys. Res. Lett., 46, 8995-9003, doi:10.1029/2019gl083812, 2019.

Duveiller, G., Forzieri, G., Robertson, E., Li, W., Georgievski, G., Lawrence, P., Wiltshire, A., Ciais, P., Pongratz, J., Sitch,
S., Arneth, A., and Cescatti, A.: Biophysics and vegetation cover change: a process-based evaluation framework for
confronting land surface models with satellite observations, Earth Syst. Sci. Data, 10, 1265-1279, doi:10.5194/essd-10-1265-
420    2018, 2018.

Findell, K. L., Gentine, P., Lintner, B. R., and Kerr, C.: Probability of afternoon precipitation in eastern United States and
Mexico enhanced by high evaporation, Nat. Geosci., 4, 434-439, doi:10.1038/ngeo1174, 2011.

Forzieri, G., Duveiller, G., Georgievski, G., Li, W., Robertson, E., Kautz, M., Lawrence, P., Garcia San Martin, L., Anthoni,
P., Ciais, P., Pongratz, J., Sitch, S., Wiltshire, A., Arneth, A., and Cescatti, A.: Evaluating the Interplay Between Biophysical
425    Processes and Leaf Area Changes in Land Surface Models, J. Adv. Model Earth Syst., 10, 1102-1126,
doi:10.1002/2018MS001284, 2018.

Forzieri, G., Miralles, D. G., Ciais, P., Alkama, R., Ryu, Y., Duveiller, G., Zhang, K., Robertson, E., Kautz, M., Martens, B.,
Jiang, C., Arneth, A., Georgievski, G., Li, W., Ceccherini, G., Anthoni, P., Lawrence, P., Wiltshire, A., Pongratz, J., Piao, S.,
Sitch, S., Goll, D. S., Arora, V. K., Lienert, S., Lombardozzi, D., Kato, E., Nabel, J. E. M. S., Tian, H., Friedlingstein, P., and
430    Cescatti, A.: Increased control of vegetation on global terrestrial energy fluxes, Nat. Clim. Change, 10, 356-362,
doi:10.1038/s41558-020-0717-0, 2020.

Gao, Y., Leung, L. R., Zhao, C., and Hagos, S.: Sensitivity of U.S. summer precipitation to model resolution and convective
parameterizations across gray zone resolutions, J. Geophys. Res. -Atmos., 122, 2714-2733, doi:10.1002/2016jd025896, 2017.

Gelaro, R., McCarty, W., Suarez, M. J., Todling, R., Molod, A., Takacs, L., Randles, C., Darmenov, A., Bosilovich, M. G.,
435    Reichle, R., Wargan, K., Coy, L., Cullather, R., Draper, C., Akella, S., Buchard, V., Conaty, A., da Silva, A., Gu, W., Kim, G.
K., Koster, R., Lucchesi, R., Merkova, D., Nielsen, J. E., Partyka, G., Pawson, S., Putman, W., Rienecker, M., Schubert, S. D.,

Sienkiewicz, M., and Zhao, B.: The Modern-Era Retrospective Analysis for Research and Applications, Version 2 (MERRA-2), J. Climate, 30, 5419-5454, doi:10.1175/JCLI-D-16-0758.1, 2017.

Hao, D., Bisht, G., Gu, Y., Lee, W.-L., Liou, K.-N., and Leung, L. R.: A parameterization of sub-grid topographical effects on

440    solar radiation in the E3SM Land Model (version 1.0): implementation and evaluation over the Tibetan Plateau, Geosci. Model Dev., 14, 6273-6289, doi:10.5194/gmd-14-6273-2021, 2021a.

Hao, Z., Hao, F., Xia, Y., Singh, V. P., Hong, Y., Shen, X., and Ouyang, W.: A Statistical Method for Categorical Drought Prediction Based on NLDAS-2, J. Appl. Meteorol. Clim., 55, 1049-1061, doi:10.1175/jamc-d-15-0200.1, 2016.

Harris, I., Osborn, T. J., Jones, P., and Lister, D.: Version 4 of the CRU TS monthly high-resolution gridded multivariate

445    climate dataset, Sci. Data, 7, 109, doi:10.1038/s41597-020-0453-3, 2020.

Hinkelman, L. M.: The Global Radiative Energy Budget in MERRA and MERRA-2: Evaluation with Respect to CERES EBAF Data, J. Climate, 32, 1973-1994, doi:10.1175/jcli-d-18-0445.1, 2019.

Huffman, G. J., Bolvin, A., Dan, B., Hsu, K., Joyce, R., and Xie, P.: NASA Global Precipitation Measurement (GPM) Integrated Multi-satellitE Retrievals for GPM (IMERG), National Aeronautics and Space Administration, 2014.

450    Jiménez, C., Prigent, C., Mueller, B., Seneviratne, S. I., McCabe, M. F., Wood, E. F., Rossow, W. B., Balsamo, G., Betts, A. K., Dirmeyer, P. A., Fisher, J. B., Jung, M., Kanamitsu, M., Reichle, R. H., Reichstein, M., Rodell, M., Sheffield, J., Tu, K., and Wang, K.: Global intercomparison of 12 land surface heat flux estimates, J. Geophys. Res., 116, doi:10.1029/2010jd014545, 2011.

Klein, S. A., and Hartmann, D. L.: The Seasonal Cycle of Low Stratiform Clouds, J. Climate, 6, 1587-1606, doi: 10.1175/1520-

455    0442(1993)006<1587:TSCOLS>2.0.CO;2, 1993.

Laloyaux, P., Balmaseda, M., Dee, D., Mogensen, K., and Janssen, P.: A coupled data assimilation system for climate reanalysis, Q. J. Roy. Meteor. Soc., 142, 65-78, doi:10.1002/qj.2629, 2016.

Lee, J. M., Zhang, Y., and Klein, S. A.: The effect of land surface heterogeneity and background wind on shallow cumulus clouds and the transition to deeper convection, J. Atmos. Sci., 76, 401–419. https://doi.org/10.1175/JAS-D-18-0196.1, 2019.

460    Lee, W. L., Liou, K. N., Wang, C. c., Gu, Y., Hsu, H. H., and Li, J. L. F.: Impact of 3-D Radiation-Topography Interactions on Surface Temperature and Energy Budget Over the Tibetan Plateau in Winter, J. Geophys. Res. -Atmos., 124, 1537-1549, doi:10.1029/2018jd029592, 2019.

Lee, X., Goulden, M. L., Hollinger, D. Y., Barr, A., Black, T. A., Bohrer, G., Bracho, R., Drake, B., Goldstein, A., Gu, L., Katul, G., Kolb, T., Law, B. E., Margolis, H., Meyers, T., Monson, R., Munger, W., Oren, R., Paw, U. K., Richardson, A. D.,

465    Schmid, H. P., Staebler, R., Wofsy, S., and Zhao, L.: Observed increase in local cooling effect of deforestation at higher latitudes, Nature, 479, 384-387, doi:10.1038/nature10588, 2011.

Liu, S., Chen, M., and Zhuang, Q.: Aerosol effects on global land surface energy fluxes during 2003–2010, Geophys. Res. Lett., 41, 7875-7881, doi:10.1002/2014gl061640, 2014.

Liu, S., Liu, X., Yu, L., Wang, Y., Zhang, G. J., Gong, P., Huang, W., Wang, B., Yang, M., and Cheng, Y.: Climate response

470    to introduction of the ESA CCI land cover data to the NCAR CESM, Clim. Dynam., 56, 4109-4127, doi:10.1007/s00382-021-05690-3, 2021.

Loeb, N. G., Kato, S., Loukachine, K., Manalo-Smith, N., and Doelling, D. R.: Angular Distribution Models for Top-of-Atmosphere Radiative Flux Estimation from the Clouds and the Earth's Radiant Energy System Instrument on the Terra Satellite. Part II: Validation, J. Atmos. Ocean Tech., 24, 564-584, doi:10.1175/jtech1983.1, 2007.

475    Loeb, N. G., Lyman, J. M., Johnson, G. C., Allan, R. P., Doelling, D. R., Wong, T., Soden, B. J., and Stephens, G. L.: Observed changes in top-of-the-atmosphere radiation and upper-ocean heating consistent within uncertainty, Nat. Geosci., 5, 110-113, doi:10.1038/ngeo1375, 2012.

Loeb, N. G., Doelling, D. R., Wang, H., Su, W., Nguyen, C., Corbett, J. G., Liang, L., Mitrescu, C., Rose, F. G., and Kato, S.: Clouds and the Earth's Radiant Energy System (CERES) Energy Balanced and Filled (EBAF) Top-of-Atmosphere (TOA)

480    Edition-4.0 Data Product, J. Climate, 31, 895-918, 10.1175/jcli-d-17-0208.1, 2018.

Ma, J., Wang, H., and Fan, K.: Dynamic downscaling of summer precipitation prediction over China in 1998 using WRF and CCSM4, Adv. Atmos. Sci., 32, 577-584, doi:10.1007/s00376-014-4143-y, 2015.

Mehran, A., AghaKouchak, A., and Phillips, T. J.: Evaluation of CMIP5 continental precipitation simulations relative to satellite-based gauge-adjusted observations, J. Geophys. Res. -Atmos., 119, 1695-1707, doi:10.1002/2013jd021152, 2014.

485    Miralles, D. G., Gentine, P., Seneviratne, S. I., and Teuling, A. J.: Land-atmospheric feedbacks during droughts and heatwaves: state of the science and current challenges, Ann. N. Y. Acad. Sci., 1436, 19-35, doi:10.1111/nyas.13912, 2019.

Mueller, B. and Seneviratne, S. I.: Systematic land climate and evapotranspiration biases in CMIP5 simulations, Geophys. Res. Lett., 41, 128-134, doi:10.1002/2013GL058055, 2014.

Oleson, K. W., Lawrence, D. M., Bonan, G. B., Flanner, M. G., Kluzek, E., Lawrence, P. J., Levis, S., Swenson, S. C., Thornton,

490    P. E., Dai, A., Decker, M., Dickinson, R., Feddema, J., Heald, C. L., Hoffman, F., Lamarque, J.-F., Mahowald, N., Niu, G.-Y., Qian, T., Randerson, J., Running, S., Sakaguchi, K., Slater, A., Stockli, R., Wang, A., Yang, Z.-L., and Zeng, X.: Technical description of version 4.0 of the Community Land Model (CLM), NCAR Technical Note NCAR/TN-478+STR, 257 pp., 2010.

Osborn, T. J., Jones, P. D., and Joshi, M.: Recent United Kingdom and global temperature variations, Weather, 72, 323–329, doi:10.1002/wea.3174, 2017.

495    Pielke, R. A.: Influence of the spatial distribution of vegetation and soils on the prediction of cumulus Convective rainfall, Rev. Geophys., 39, 151-177, doi:10.1029/1999rg000072, 2001.

Pitman, A. J.: The evolution of, and revolution in, land surface schemes designed for climate models, Int. J. Climatol., 23, 479-510, doi:10.1002/joc.893, 2003.

Rieck, M., Hohenegger, C., and van Heerwaarden, C. C.: The Influence of Land Surface Heterogeneities on Cloud Size

500    Development, Mon. Weather Rev., 142, 3830-3846, doi:10.1175/mwr-d-13-00354.1, 2014.

Rochetin, N., Couvreux, F., and Guichard, F.: Morphology of breeze circulations induced by surface flux heterogeneities and their impact on convection initiation, Q. J. Roy. Meteor. Soc., 143, 463-478, doi:10.1002/qj.2935, 2017.

Rodell, M., Houser, P. R., Jambor, U., Gottschalck, J., Mitchell, K., Meng, C. J., Arsenault, K., Cosgrove, B., Radakovich, J., Bosilovich, M., Entin, J. K., Walker, J. P., Lohmann, D., and Toll, D.: The Global Land Data Assimilation System, B. Am.
505 Meteorol. Roc., 85, 381-394, doi:10.1175/bams-85-3-381, 2004.

Rotenberg, E. and Yakir, D.: Contribution of semi-arid forests to the climate system, Science, 327, 451–454, doi:10.1126/science.1179998, 2010.

Saha, S., Moorthi, S., Wu, X., Wang, J., Nadiga, S., Tripp, P., Behringer, D., Hou, Y.-T., Chuang, H.-y., Iredell, M., Ek, M., Meng, J., Yang, R., Mendez, M. P., van den Dool, H., Zhang, Q., Wang, W., Chen, M., and Becker, E.: The NCEP Climate
510 Forecast System Version 2, J. Climate, 27, 2185-2208, doi:10.1175/jcli-d-12-00823.1, 2014.

Sohn, B.-J.: Cloud-induced infrared radiative heating and its implications for large-scale tropical circulations, J. Atmos. Sci., 56, 2657-2672, doi:10.1175/1520-0469(1999)056<2657:CIIRHA>2.0.CO;2, 1999.

Stone, D. A., Risser, M. D., Angélil, O. M., Wehner, M. F., Cholia, S., Keen, N., Krishnan, H., O'Brien, T. A., and Collins, W. D.: A basis set for exploration of sensitivity to prescribed ocean conditions for estimating human contributions to extreme
515 weather in CAM5.1-1degree, Weather and Climate Extremes, 19, 10-19, doi:10.1016/j.wace.2017.12.003, 2018.

Sun, W., Li, L., and Wang, B.: Reducing the biases in shortwave cloud radiative forcing in tropical and subtropical regions from the perspective of boundary layer processes, Sci. China Earth Sci., 59, 1427-1439, doi:10.1007/s11430-016-5290-z, 2016.

Lothon, M., Campistron, B., Chong, M., Couvreux, F., Guichard, F., Rio, C., and Williams, E.: Life Cycle of a Mesoscale Circular Gust Front Observed by a C-Band Doppler Radar in West Africa, Mon. Weather Rev., 139, 1370-1388. doi:
520 10.1175/2010MWR3480.1, 2011.

Novick, K. A., Biederman, J. A., Desai, A. R., Litvak, M. E., Moore, D. J. P., Scott, R. L., and Torn, M. S.: The AmeriFlux network: A coalition of the willing, Agr. Forest Meteorol., 249, 444-456, doi:10.1016/j.agrformet.2017.10.009, 2018.

Sun, Q., Miao, C., Duan, Q., Ashouri, H., Sorooshian, S., and Hsu, K. L.: A Review of Global Precipitation Data Sets: Data Sources, Estimation, and Intercomparisons, Rev. Geophys., 56, 79-107, doi:10.1002/2017rg000574, 2018.

525 Sun, W., Wang, B., Wang, Y., Zhang, G. J., Han, Y., Wang, X., and Yang, M.: Parameterizing Subgrid Variations of Land Surface Heat Fluxes to the Atmosphere Improves Boreal Summer Land Precipitation Simulation with the NCAR CESM1.2, Geophys. Res. Lett., 48, doi:10.1029/2020gl090715, 2021.

Tang, Y., Wen, X., Sun, X., and Wang, H.: Interannual variation of the Bowen ratio in a subtropical coniferous plantation in southeast China, 2003-2012, PLoS One, 9, e88267, doi:10.1371/journal.pone.0088267, 2014.

530 Taylor, C. M., Parker, D. J., and Harris, P. P.: An observational case study of mesoscale atmospheric circulations induced by soil moisture, Geophys. Res. Lett., 34, doi:10.1029/2007gl030572, 2007.

Waliser, D. E., Moncrieff, M. W., Burridge, D., Fink, A. H., and Yuter, S.: The ''year'' of tropical convection (May 2008– April 2010): Climate variability and weather highlights. B. Am. Meteorol. Soc., 93, 1189–1218, doi:10.1175/2011bams3095.1, 2012.

535 Wang, Y., Zhang, G. J., and Craig, G. C.: Stochastic convective parameterization improving the simulation of tropical precipitation variability in the NCAR CAM5, Geophys. Res. Lett., 43, 6612-6619, doi:10.1002/2016gl069818, 2016.

Wang, Y., Zhang, G. J., and He, Y. J.: Simulation of Precipitation Extremes Using a Stochastic Convective Parameterization in the NCAR CAM5 Under Different Resolutions, J. Geophys. Res. -Atmos., 122, doi:10.1002/2017jd026901, 2017.

Wang, Y., Zhang, G. J., and Jiang, Y.: Linking Stochasticity of Convection to Large-Scale Vertical Velocity to Improve Indian

540    Summer Monsoon Simulation in the NCAR CAM5, J. Climate, 31, 6985-7002, doi:10.1175/jcli-d-17-0785.1, 2018.

Wang, Y., Xia, W., Liu, X., Xie, S., Lin, W., Tang, Q., Ma, H.-Y., Jiang, Y., Wang, B., and Zhang, G. J.: Disproportionate control on aerosol burden by light rain, Nat. Geosci., 14, 72-76, doi:10.1038/s41561-020-00675-z, 2021a.

Wang, Y., Zhang, G. J., Xie, S., Lin, W., Craig, G. C., Tang, Q., and Ma, H.-Y.: Effects of coupling a stochastic convective parameterization with the Zhang–McFarlane scheme on precipitation simulation in the DOE E3SMv1.0 atmosphere model,

545    Geosci. Model Dev., 14, 1575-1593, doi:10.5194/gmd-14-1575-2021, 2021b.

Wei, L., Wang, Y., Liu, S., Zhang, G. J., and Wang, B.: Distinct roles of land cover in regulating spatial variabilities of temperature responses to radiative effects of aerosols and clouds, Environ. Res. Lett., 16, doi:10.1088/1748-9326/ac3f04, 2021.

Xia, Y., Hao, Z., Shi, C., Li, Y., Meng, J., Xu, T., Wu, X., and Zhang, B.: Regional and Global Land Data Assimilation Systems: Innovations, Challenges, and Prospects, J. Meteorol. Res-Prc., 33, 159-189, doi:10.1007/s13351-019-8172-4, 2019.

550    Yu, R., Li, J., Zhang, Y., and Chen, H.: Improvement of rainfall simulation on the steep edge of the Tibetan Plateau by using a finite-difference transport scheme in CAM5, Clim. Dynam., 45, 2937-2948, doi:10.1007/s00382-015-2515-3, 2015.

Yue, S., Yang, K., Lu, H., Zhou, X., Chen, D., and Guo, W.: Representation of Stony Surface-Atmosphere Interactions in WRF Reduces Cold and Wet Biases for the Southern Tibetan Plateau, J. Geophys. Res. -Atmos., 126, doi:10.1029/2021jd035291, 2021.

555    Zaitchik, B. F., Rodell, M., and Olivera, F.: Evaluation of the Global Land Data Assimilation System using global river discharge data and a source-to-sink routing scheme, Water Resour. Res., 46, doi:10.1029/2009wr007811, 2010.

Zhou, X., Yang, K., Beljaars, A., Li, H., Lin, C., Huang, B., and Wang, Y.: Dynamical impact of parameterized turbulent orographic form drag on the simulation of winter precipitation over the western Tibetan Plateau, Clim. Dynam., 53, 707-720, doi:10.1007/s00382-019-04628-0, 2019.

560    Zhou, X., Yang, K., Ouyang, L., Wang, Y., Jiang, Y., Li, X., Chen, D., and Prein, A.: Added value of kilometer-scale modeling over the third pole region: a CORDEX-CPTP pilot study, Clim. Dynam., 57, 1673-1687, doi:10.1007/s00382-021-05653-8, 2021.

Hao, D., Bisht, G., Huang, M., Ma, P.-L., Tesfa, T. K., Lee, W.-L., Gu, Y., Leung, R. L.: Impacts of sub-grid topographic representations on surface energy balance and boundary conditions in the E3SM Land Model. ESSPAr[preprint],

565    https://doi.org/10.1002/essoar.10508175.1, 08 October 2021b.